RSC Advances

PAPER

View Article Online
View Journal | View Issue

Cite this: *RSC Adv.*, 2025, **15**, 36749

Structural, morphological, dielectric and semiconducting properties of ZnO nanoparticles calcined at 500 °C

Anurag Yadav,[a] A. G. Varshan,[a] Silu Nayak,[a] Jing-Yun Wu *[b] and Pounraj Thanasekaran *[a]

Received 23rd August 2025
Accepted 25th September 2025

DOI: 10.1039/d5ra06276d

rsc.li/rsc-advances

Metal oxide semiconductors (MOS) occupy a prominent position in both academic research and industrial applications owing to their diverse and distinctive properties, including electrical, optical, mechanical, magnetic, and electrochromic characteristics. In this study, we focused on zinc oxide nanoparticles (ZnO NPs) synthesized *via* a cost-effective co-precipitation method. Characterization techniques such as FT-IR, powder XRD, XPS, and UV-vis spectroscopy confirmed the successful synthesis of ZnO NPs, which exhibited an optical band gap of approximately 3.16 eV. Dielectric studies showed a dielectric constant value of ~98 at 10^3 Hz, remaining stable at higher frequencies due to reduced charge accumulation at grain boundaries. Impedance spectroscopy indicated that increasing temperature decreased the semicircle radius in Cole–Cole plots, reflecting enhanced charge carrier mobility and confirming semiconducting behavior. The AC conductivity ranged from 10^{-8} to 10^{-5} S cm^{-1}, slightly increasing with frequency, suggesting improved charge carrier mobility. These findings underline the promising potential of ZnO NPs for advanced technological applications, particularly in spintronic devices and UV photodetectors.

1. Introduction

Zinc oxide (ZnO) nanoparticles (NPs) have emerged as one of the most versatile semiconductor nanomaterials due to their distinctive properties, including wide band gap semiconductivity, optical transparency, chemical stability, and piezoelectric characteristics. Crystallizing in a thermodynamically stable hexagonal wurtzite phase, ZnO exhibits strong ionic bonding between Zn^{2+} and O^{2-} ions, which underpins its wide direct band gap (~3.37 eV), high exciton binding energy (~60 meV), substantial electron mobility, and excellent thermal and mechanical stability.[1–4] These intrinsic properties have positioned ZnO as a promising candidate for a wide range of applications, including ultraviolet (UV) photodetectors, transparent electronics, gas sensors, solar cells, supercapacitors, piezoelectric nanogenerators and light-emitting diodes (LEDs).[5–17] Furthermore, ZnO can serve as a photocatalyst for biodiesel production through the esterification and transesterification of fatty acids and oils, thereby broadening its applications in energy harvesting and environmental technologies.[18] Beyond electronic and optoelectronic applications, ZnO NPs exhibit notable antimicrobial activity through reactive oxygen species generation, Zn^{2+} ion release, and membrane disruption. Their broad-spectrum efficacy and relatively low cytotoxicity make them promising alternatives to conventional antibiotics and bactericides.[19,20]

ZnO nanostructures with diverse sizes, morphologies, and crystal structures have been synthesized using various techniques, including hydrothermal,[21] solvothermal,[22] co-precipitation,[23] sonochemical,[24] sol–gel,[25] microemulsion,[26] chemical vapor deposition,[27] thermal decomposition,[28] microwave irradiation,[29] and laser ablation.[30] Among them, co-precipitation is particularly attractive due to its simplicity, scalability, and cost-effectiveness.[23] These methods influence key parameters such as crystallite size, defect density, morphology, and compositional purity that directly affect the physical, thermal, and chemical properties of ZnO nanoparticles.[31] Calcination temperature is critical for achieving high phase purity, controlling crystallite growth, and stabilizing the wurtzite phase. Annealing at 500 °C has been shown to significantly improve crystal quality by reducing structural defects, thereby enhancing the optical properties of ZnO NPs.[32–34] A key strategy for optimizing ZnO NPs for optoelectronic applications involves tuning their band gap and carrier dynamics through methods such as doping or nanostructuring. The incorporation of foreign elements into the ZnO NPs lattice can introduce localized states or modify native defect concentrations, while reducing particle size to the nanoscale can induce quantum confinement effects.[35] These modifications have been shown to

[a]*Department of Chemistry, Pondicherry University, Puducherry 605014, India. E-mail: ptsekaran.chem@pondiuni.ac.in; Tel: +91-413-2654-413*
[b]*Department of Applied Chemistry, National Chi Nan University, Nantou 545, Taiwan. E-mail: jyunwu@ncnu.edu.tw*

Table 1 Reported ZnO NP studies on dielectric, impedance and conducting properties[a]

S. no.	Methods (calcination, °C)	Crystalline size of ZnO (nm)	κ, T (K)	tan δ	σ_{AC} (S cm^{-1})	E_g (eV)	Impedance data	Ref.
1	Co-precipitation (400)	43	∼100 (80–300)	∼10	$\sim 1 \times 10^{-4}$	n.r	n.r	41
2	Electrochemical deposition (350)	20.09	n.r	n.r	n.r	3.24	R_1 = n.r [a]$R_2 = 4.21 \times 10^4$ [b]CPE $= 1.60 \times 10^{-5}$	80
3	Conventional sintering (700)	∼50	n.r	n.r	1×10^{-8}	n.r	n.r	81
4	Emulsion precipitation (400)	38.1–76.9	1×10^4 (298)	n.r	1×10^{-5}	n.r	n.r	82
5	Pristine and green-synthesis[c]	17.5–23.3	58–27 613 (297–459)	0.19–0.63	2.88×10^{-5}	n.r	n.r	83
6	Pressure-less solid-state reaction (1000)	n.r	1.9×10^5 (298)	1×10^2	1.24×10^{-5}	n.r	n.r	84
7	ZnO-1200 (commercial ZnO powder) (1200)	n.r	1.9×10^4 (293–363)	9.2	n.r	n.r	[d]$R_1 = 1.27 \times 10^2$ [d]$R_2 = 5.52 \times 10^2$ [d]$R_3 = 2.83 \times 10^4$ [d]$R_4 = 4.95 \times 10^3$ [e]CPE$_2 = 1.10 \times 10^{-10}$ [e]CPE$_3 = 6.94 \times 10^{-9}$ [e]CPE$_4 = 7.61 \times 10^{-8}$	85
8	Chemical precipitation[f]	∼17	∼90 (303–383)	∼10	$\sim 25 \times 10^{-5}$	n.r	n.r	86
9	Precipitation[g] (100)	∼19	25.59 (80–300)	0.809	11.9×10^{-5}	n.r	n.r	87
10	Precipitation (850)	∼20	∼500 (300–523)	∼350	$\sim 1.4 \times 10^{-3}$	2.36	n.r	88
11	Co-precipitation (500)	7–24	97.74, (170–350)	0.96	5.03×10^{-5}	3.16	[h]$R_1 = 2.68 \times 10^7$ [h]$R_2 = 1.76 \times 10^6$ [i]CPE $= 7.21 \times 10^{-7}$	This work

[a] Abbreviations used: dielectric constant (κ); dielectric loss (tan δ); AC conductivity (σ_{AC}); band gap (E_g); temperature (T); resistance (R); Constant Phase Element (CPE); [a]ohm cm^2; [b]F s^{-1}; [c]pinwheel capping agent; [d,e]n.r = not reported; [f]starch capping agent; [g]soluble starch stabilizing agent; [h]ohm; [i](S s^n).

significantly improve the electrical, magnetic, photocatalytic, and luminescent behavior of ZnO nanomaterials.[36–39]

According to research findings, the dielectric and AC electrical properties of ZnO NPs are closely linked to microstructural features such as crystallite size, grain boundaries, and lattice defects, as well as the presence of additional charge carriers.[8,40–43] Especially, dielectric permittivity is governed by interfacial (Maxwell–Wagner) and orientation (dipolar) polarization, while AC conductivity arises from charge carrier hopping and defect-mediated transport mechanisms.[37,42,43] Grain boundaries, in particular, act as charge trapping sites and influence space-charge (interfacial) polarization, particularly at low frequencies, which in turn affects both dielectric constant and loss characteristics.[27] These properties can change significantly when ZnO NPs are doped or alloyed with other metals or materials.[8,36,42,43] Variations in nanoparticle size can also lead to changes in the dielectric constant.[8,23,44] The large dielectric loss observed at low frequencies is typically attributed to impurities and crystal defects within the ZnO NPs. Moreover, in composite systems, both the dielectric constant and dielectric loss generally increase with increasing particle size.[45]

Despite extensive literature on ZnO nanostructures, there remains significant scope for further investigation, particularly regarding their potential applications. Especially, limited reports systematically correlate synthesis temperature, crystallite size, morphology, dielectric/conducting behavior and bandgap of pure ZnO NPs (Table 1). This study aims to fill that gap and to explore the applicability of ZnO nanoparticles calcined at 500 °C in terms of dielectric permittivity, conductivity and bandgap. Zinc oxide nanoparticles (ZnO NPs) were synthesized *via* a simple and cost-effective chemical precipitation method, followed by calcination at 500 °C. The structural, morphological, and compositional features of the ZnO NPs were characterized using FT-IR, PXRD, FE-SEM, and EDX analyses. Temperature- and frequency-dependent dielectric permittivity and dielectric loss, and electrical conductivity, along with the optical band gap, were systematically investigated and compared with values reported for ZnO NPs by other research groups (Table 1). Notably, doping ZnO nanoparticles with metals or carbon-based materials would significantly enhance their dielectric constant and electrical conductivity, thereby making such modified compositions promising candidates for advanced energy storage applications.

2. Experimental section

2.1 Materials

All reagents were of analytical grade and used as received without further purification. Zinc nitrate hexahydrate ($Zn(NO_3)_2 \cdot 6H_2O$), sodium hydroxide (NaOH), and ethanol (EtOH) were purchased from Merck (India). Double-distilled water was used for all solution preparations.

2.2 Preparation of ZnO NPs

ZnO nanoparticles were synthesized *via* a simple co-precipitation method.[46] In a typical procedure, 0.1 M aqueous solution of $Zn(NO_3)_2 \cdot 6H_2O$ (298 mg) was prepared and stirred magnetically at room temperature for 30 min. Aqueous NaOH (0.2 M) was then added dropwise to the zinc nitrate solution under continuous stirring until the pH reached ~10. A white precipitate of zinc hydroxide ($Zn(OH)_2$) formed immediately. The mixture was stirred for an additional 2 h to ensure complete reaction. The resulting precipitate was separated by centrifugation, washed several times with distilled water and ethanol to remove residual ions and by-products, and then dried in a hot air oven at 80 °C overnight. The dried powder was subsequently calcined at 500 °C in a muffle furnace for 6 h in air to obtain phase-pure ZnO nanoparticles.

2.3 Characterization

Powder X-ray diffraction (PXRD) measurements were performed using a Bruker D8 Advance diffractometer equipped with Cu Kα radiation ($\lambda = 1.5406$ Å), and operated at 40 kV and 40 mA.

The crystallite size was estimated using the Debye–Scherrer equation. FT-IR spectra were recorded on a Nicolet iS10 from Thermo Fisher Scientific using the KBr pellet method in the range of 4000–400 cm^{-1}. Scanning electron microscopy (SEM) images were obtained using a JEOL JSM-6610 series scanning electron microscope at an operating voltage of 30 kV to analyze surface morphology and particle aggregation. X-ray photoelectron spectroscopy (XPS) measurements were performed using a PHI Versa Probe III scanning XPS microprobe with Al Kα radiation (1486.6 eV) for surface chemical state analysis. UV-Vis-NIR absorption spectra were collected using a Shimadzu UV-3600 Plus UV-Vis-NIR spectrophotometer in the wavelength range of 200–2500 nm. X-ray photoelectron spectrometer measurements were carried out using a Thermo Scientific K-Alpha analyzer, which features a 180° double focusing hemispherical analyzer with a 128-channel detector, an Al Kα micro-focused monochromator with a variable spot size, and an ion gun with an energy range of 100–4000 eV. Particle size analysis was conducted using a Malvern Zeta Sizer Ver. 8.02 (serial number: MAL1043157).

2.4 Electrical measurements

A broadband dielectric spectroscopy (Model-Concept 80) measurement was conducted using a Novocontrol (GmbH, Germany) Alpha Analyzer over a wide frequency range from 10^3 Hz to 10^6 Hz and a temperature range from 170 K to 350 K. The experiment involved applying an AC electric field to the pellet form of ZnO NPs placed between two parallel circular copper plates (diameter = 20 mm) separated by 0.1 mm Teflon spacers at 25 °C. The temperature was controlled by a Novocontrol Quatro Cryosystem, which maintains temperature stability better than 0.1 K. Impedance spectroscopy has been extensively used to study the physical processes that determine complex electrical functions such as dielectric permittivity and conductivity. The real (ε') and imaginary (ε'') parts of the dielectric permittivity of ZnO NPs are calculated based on the following eqn (1) and (2):

$$\varepsilon' = \frac{Ct}{\varepsilon_0 A} \quad (1)$$

$$\varepsilon'' = \varepsilon' \tan \delta \quad (2)$$

where C is the capacitance in farads, F, t is the sample thickness in centimetre, A is the cross-sectional area in cm^2, and ε_0 is the permittivity of free space, equal to $\varepsilon_0 = 8.854 \times 10^{-14}$ F cm^{-1}. The AC conductivity (σ_{AC}) was calculated by eqn (3)

$$\sigma_{AC} = L/(RS) \quad (3)$$

where R (Ω) was obtained from arc extrapolation to the Z' axis on the Nyquist curve. L and S are the thickness and surface area of the sample, respectively.

3. Result and discussion

3.1 Characterization

The FTIR spectrum of the synthesized ZnO NPs calcined at 500 °C was determined in the region of 500–4000 cm^{-1}, as shown in Fig. S1. Five major IR modes were noted at 559, 1352, 1385, 1598, and 3427 cm^{-1}. The peak observed in the range of 500–800 cm^{-1} was attributed to the characteristic ZnO stretching vibration, which serves as a good evidence for the formation and stabilization of ZnO NPs.[47] The bands observed at 1598 and 3427 cm^{-1} were due to the stretching vibration of the OH group present in physically absorbed water, which may have been introduced during pellet preparation.[48] The peaks at 1352 and 1385 cm^{-1} were associated with the bending vibrational mode of the OH group found in methanol, which could have been present after washing the NPs.[49]

The powder XRD pattern of the ZnO NPs calcined at 500 °C (Fig. 1) provided evidence for their crystalline nature and hexagonal phase, with the lattice parameters of $a = b = 3.2494$ Å and $c = 5.2108$ Å and space group $P6_3mc$. No impurities were detected, which is consistent with the standard JCPDS file (036-1451) (Tables S1–S5). The values of the ZnO lattice parameters (a, b and c) are determined using eqn (4):[50]

$$\frac{1}{d_{(hkl)}^2} = \frac{4}{3}\left[\frac{h^2 + hk + k^2}{a^2}\right] + \frac{l^2}{c^2} \quad (4)$$

where d is the interplanar distance and h, k, l are the Miller indices.

The average crystallite size (D) calculated using Debye–Scherrer's eqn (5) was ~15.8 nm. This value aligns with the previous report for ZnO NPs,[51] confirming the reliability of the Debye–Scherrer method for estimating nanoparticle dimensions.

$$D = 0.94\lambda/\beta \cos \theta \quad (5)$$

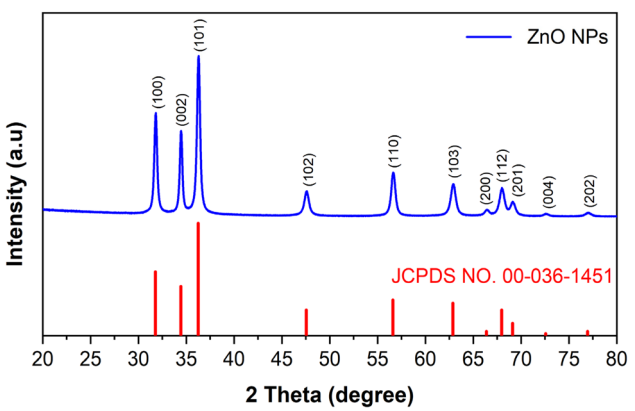

Fig. 1 PXRD pattern of the ZnO NPs calcined at 500 °C, confirming a hexagonal wurtzite phase.

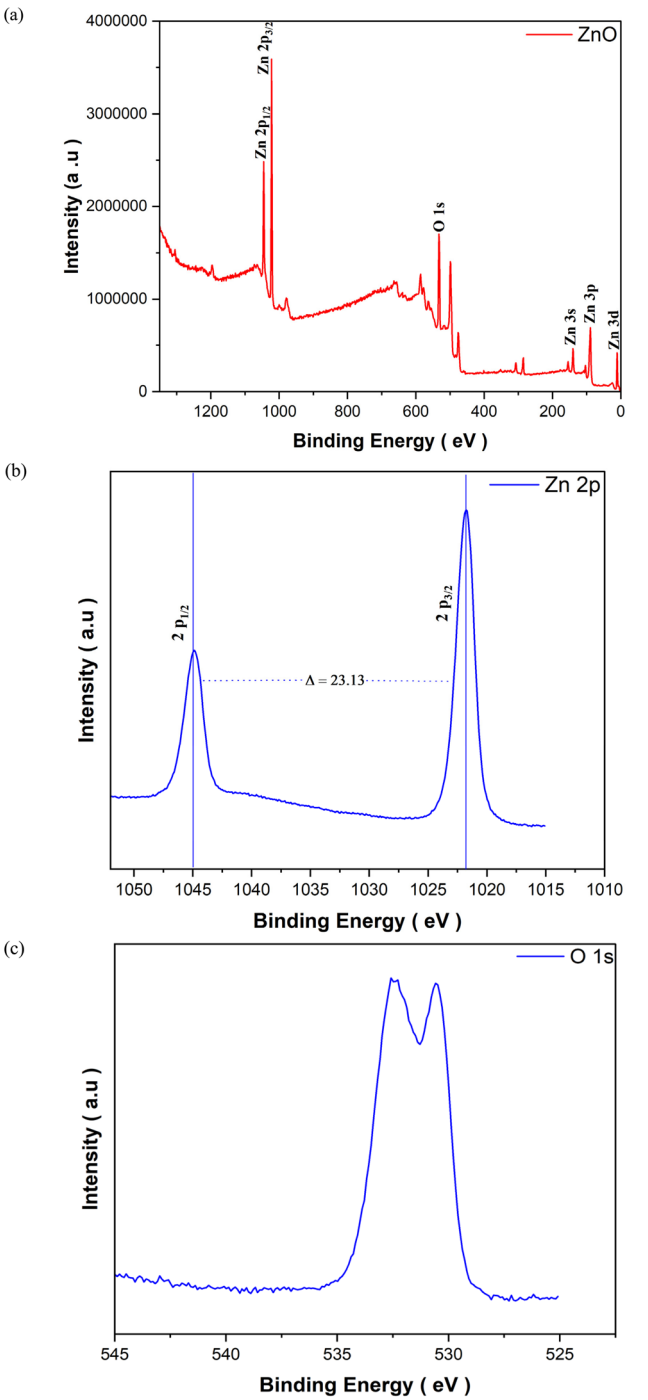

Fig. 2 (a) XPS survey spectrum of the ZnO NPs calcined at 500 °C; (b and c) XPS core level scan of Zn 2p and O 1s.

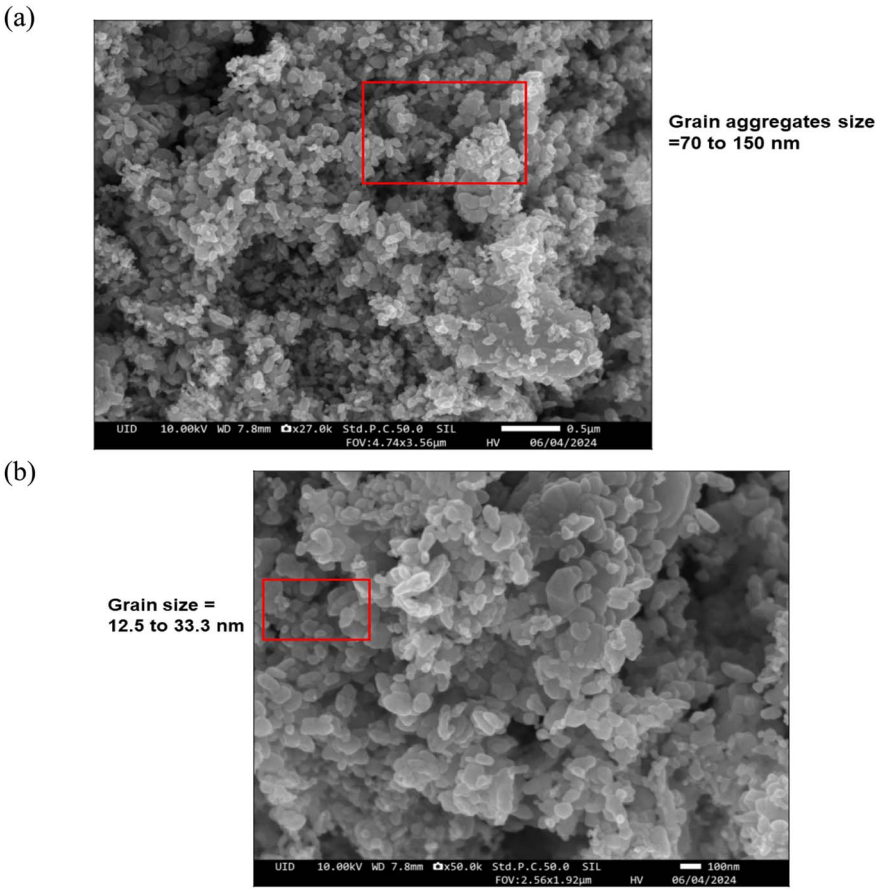

Fig. 3 SEM images of ZnO NPs calcined at 500 °C. (a) Low-magnification image revealing nanoparticle aggregation; (b) high-magnification view showing polyhedral to nearly spherical morphology and grain-boundary features.

where λ is the incident X-ray wavelength (CuKα = 1.54056 Å), β is the full width at half maximum (FWHM) of the respective peak and θ represents the Bragg angle of diffraction.

The surface element compositions of the ZnO NPs calcined at 500 °C were characterized using X-ray photoelectron spectrometer (XPS) analysis, as shown in Fig. 2. The XPS survey spectrum revealed high signals for zinc and oxygen elements, confirming the successful formation of ZnO NPs.[52] The binding energies of the Zn 2p spectral peaks were found to be 1021.9 and 1045.1 eV, for Zn $2p_{3/2}$ and Zn $2p_{1/2}$, respectively. Additionally, the peak at 532.1 eV corresponds to oxygen ions within the ZnO lattice, while the peak at 530.6 eV is attributed to the presence of OH on the surface. These results collectively confirm the presence of ZnO NPs and their characteristic surface compositions.

Scanning electron microscopy (SEM) was employed to investigate the morphology of the ZnO NPs at varying magnifications (Fig. 3). At low magnification (Fig. 3a), the particles appeared as agglomerated clusters arranged in a porous structure. The grains exhibited irregular shaped and varied in size, forming loosely packed aggregates.[41,44,53] Numerous voids and intergranular spaces were visible, acting as grain boundaries, although these boundaries were less well-defined at this magnification (Fig. S4). Most grains measured approximately 26–181 nm in diameter, while some larger features, up to ~200 nm, likely corresponded to fused or overlapping crystallites rather than individual grains. In contrast, the individual grains became more distinct, displaying morphologies that range from polyhedral to nearly spherical at high magnification (Fig. 3b). The grains, measuring approximately 12.5 to 33.3 nm, exhibited a nanoscale morphology with well-defined boundaries (Fig. S4), in good agreement with the crystallite size determined from PXRD analysis. The surfaces of the grains appeared clean and smooth, indicating crystalline growth during calcination at 500 °C. Based on the morphological features, it is suggested that a nanocrystalline network in which well-defined grain boundaries separate crystalline domains provides a large specific surface area and numerous interfacial sites for charge trapping.[54,55] These observations may support the inference of grain boundary-driven dielectric behavior, as noted in the impedance and dielectric measurements (*vide infra*).

Fig. S2 presents the EDX analysis of the elemental composition of ZnO NPs calcined at 500 °C. The analysis confirmed the presence of zinc (Zn), oxygen (O) and carbon (C, due to carbon tape during the measurement) with no specified impurities detected. Particle size analysis further corroborated that the ZnO NPs calcined at 500 °C were in the nanoscale range, with particle sizes varying from 78 to 142 nm,[56] as illustrated in

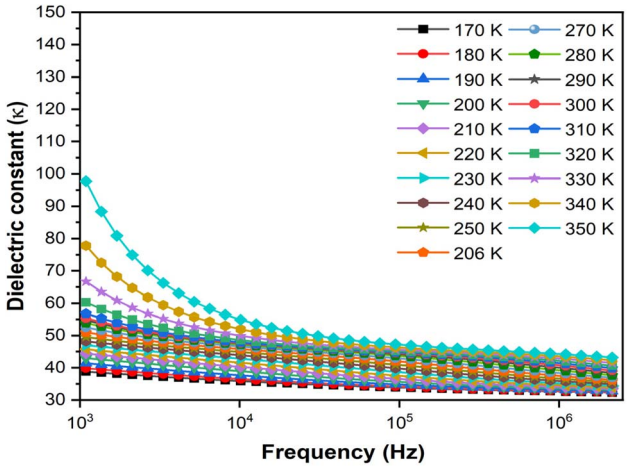

Fig. 4 Dielectric constant (κ) *versus* frequency for ZnO NPs calcined at 500 °C, measured at various temperatures (170–350 K).

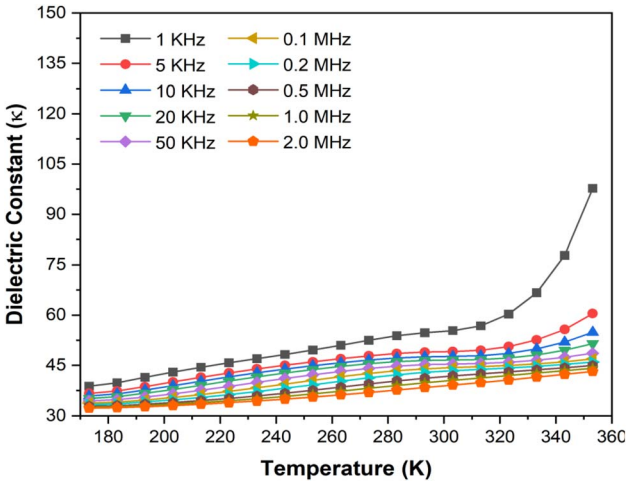

Fig. 5 Dielectric constant (κ) *versus* temperature for ZnO NPs calcined at 500 °C, measured at various frequencies (10^3 to 10^6 Hz).

Fig. S3. This finding aligns with the XRD pattern, which indicates that the synthesized ZnO NPs exhibited good crystallinity.

3.2 Dielectric permittivity

The dielectric properties of ZnO NPs displayed significant improvements due to the presence of interfacial and orientation polarizations at low and high frequencies, respectively.[57] Fig. 4 presents the frequency dependent (10^3 to 10^6 Hz) dielectric constant (κ) of ZnO NPs calcined at 500 °C under measurement temperatures ranging from 170 to 350 K. At low frequency (10^3 Hz), the dielectric (κ) of ZnO NPs was ~98, gradually decreasing with increasing the frequency until reaching a plateau at high frequencies. This plateau may be attributed to the slower movement of charges and reduced charge accumulation at grain boundaries within the dielectric material.[58] In general, dielectric materials consist of strongly conducting grains and poorly conducting grain boundaries. In ZnO NPs, charge accumulation can occur due to several factors, including the grains, grain boundaries, the presence of defects (such as oxygen vacancies and interfacial dislocations), and various polarizations. This accumulation leads to complete polarization in response to the applied electric field, which explains the increased relative κ values observed at lower frequencies.[59,60] However, at high frequencies, electric dipoles struggle to respond adequately to the changing electric field. Factors such as slower charge movement, reduced charge accumulation at grain boundaries (which act as traps or barriers), and the presence of space charge polarization at these boundaries contribute to the observed decrease in the dielectric constant (κ).[58]

The effect of temperature on the dielectric response was also measured, with results shown in Fig. 5. As the temperature increased, the dielectric constant (κ) varied, peaking at 350 K (10^3 Hz). This increase in dielectric constant (κ = ~98) is attributed to enhanced thermal vibrations and increased molecular motion, which facilitate more efficient polarization against the applied electric field.[37,61]

3.3 Dielectric loss

The dielectric loss, also known as tangent loss, in dielectric materials refers to the dissipation of energy as heat when polarization lags behind the applied electric field. This phenomenon is significantly influenced by impurities and imperfections within the crystal lattice.[62] Typically, dielectric loss arises from several mechanisms, including interfacial polarization (due to space charge migration), direct current (DC) conduction, and molecular dipole movement, commonly referred to as dipole loss.[63] Fig. 6a illustrates the frequency dependence of the dielectric loss ($\tan\delta$) for ZnO NPs calcined at 500 °C, measured over a temperature range of 170–350 K. At lower frequencies, the dielectric loss significantly increased, reaching a value of 0.98 at 10^3 Hz. This increase can be attributed to the sluggish response of molecular orientations to the applied electric field, along with charge accumulation at interfaces and interfacial polarization.[64] Conversely, at higher frequencies, the dipoles within the ZnO NPs encountered difficulties in aligning effectively with the applied field. Consequently, the ability of ZnO NPs to dissipate energy as dielectric loss diminished. This behavior underscores the complex interplay between frequency, molecular orientation, and dielectric properties in ZnO NPs. Fig. 6b shows the temperature dependence of the dielectric loss ($\tan\delta$) for ZnO NPs calcined at 500 °C, measured over the frequency range of 10^3 to 10^6 Hz. At low temperatures (<250 K), the dielectric loss remained nearly independent of temperature. However, at around 350 K, a significant increase in dielectric loss was observed, which can be attributed to space charge polarization and interfacial polarization effects. The relatively low dielectric loss at higher frequencies indicates that ZnO NPs are promising candidates for high-frequency device applications.

3.4 Impedance spectra analysis

The impedance characteristics of the materials provide precise predictions regarding the contributions of grains, grain

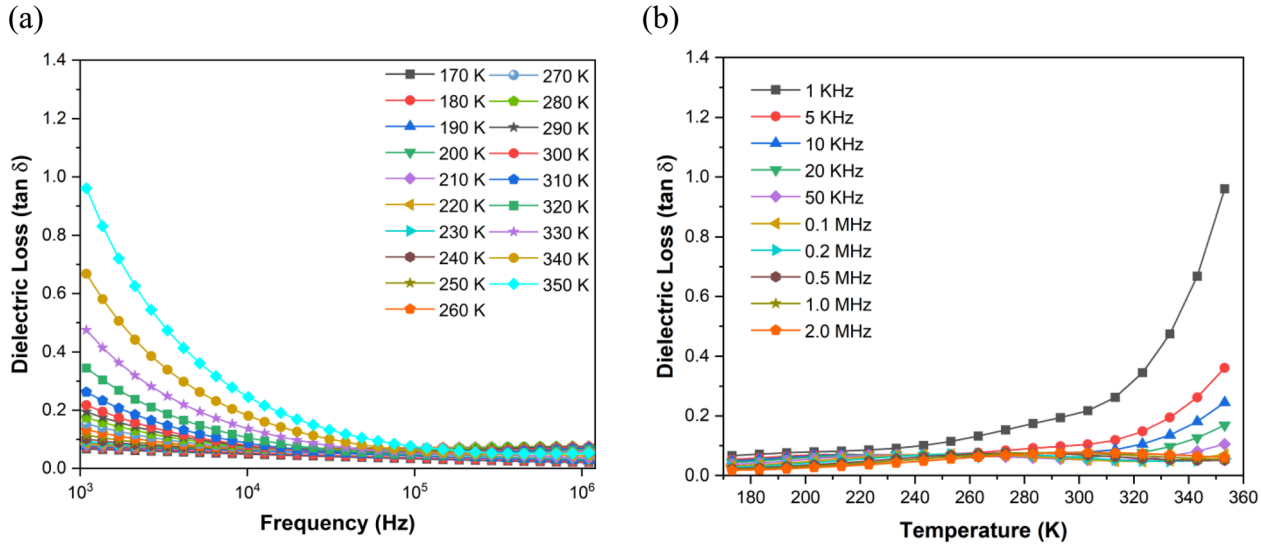

Fig. 6 (a) Dielectric loss (tan δ) *versus* frequency for ZnO NPs calcined at 500 °C, recorded over the measurement temperature range of 170–350 K and (b) dielectric loss (tan δ) *versus* temperature for ZnO NPs calcined at 500 °C, recorded over the measurement frequency range of 10^3 to 10^6 Hz.

boundaries, and electrode–material interfaces during charge transport in the material under investigation.[65] The impedance analysis diagram for ZnO NPs calcined at 500 °C is obtained by plotting the imaginary component of impedance (Z'') against the real component of impedance (Z') over a frequency range of 10^3 to 10^7 Hz and a wide temperature range of 170–350 K (see Fig. 7, Cole–Cole plot). In Fig. 7, the symbols represent the experimental data, while the solid line represents the fitted data. An incomplete semicircle is observed below 220 K, indicating that the ZnO NPs may lack sufficient thermal energy to overcome potential barriers or initiate dynamic processes that affect charge carriers.[66] As the temperature increased, a fully resolved semicircle emerged, demonstrating a decrease in resistance at higher temperatures, which reflects the impedance characteristics. The rise in temperature led to an increase in charge carrier mobility due to the additional thermal energy, resulting in a semicircle with a decreasing radius in the Cole–Cole plot, which is indicative of typical semiconductor behavior. The reduction in the semicircle radius is attributed to the enhanced charge carrier mobility facilitated by the increased thermal energy as the temperature rises.

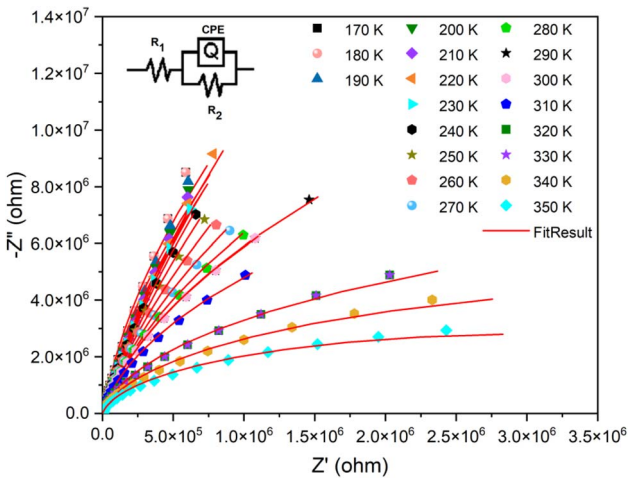

Fig. 7 Nyquist plots (Z'' *vs.* Z') of ZnO NPs calcined at 500 °C, measured between 170–350 K (Inset: equivalent circuit model used for fitting impedance spectra).

The findings from the impedance study were validated by fitting the experimental data to a theoretical electrical equivalent circuit model using ZsimpWin 2.0 software. This approach confirms the validity of the theoretical model in demonstrating the electrical properties of the materials. In this equivalent circuit, R_1 typically represents the series resistance associated with the external circuit elements,[67] while R_2 denotes the charge transfer resistance,[68] which is often linked to the interfacial electron transfer process rather than grain resistance. Additionally, the constant phase element (CPE) accounts for deviations in grain capacitance. The measured Electrochemical Impedance Spectroscopy (EIS) data at selected temperatures were analyzed using ZsimpWin software to obtain the values of series resistance (R_1), grain resistance (R_2), and grain capacitance (CPE), as represented in Table S6. Based on this analysis, we concluded that the electrical properties of ZnO NPs are predominantly influenced by grain boundary effects rather than grain (bulk) characteristics (Fig. S5).[69,70]

3.5 AC conductivity

To investigate the electrical property of the ZnO NPs calcined at 500 °C, we measured the frequency-dependent electrical conductivity as a function of temperature. The AC conductivity (σ_{AC}) measurement indicated that the temperature-dependent electrical conductivity of ZnO NPs calcined at 500 °C increased from 10^{-8} to 10^{-5} S cm^{-1} measured over a frequency range of 10^3 to 10^6 K (Fig. 8). This phenomenon is observed in

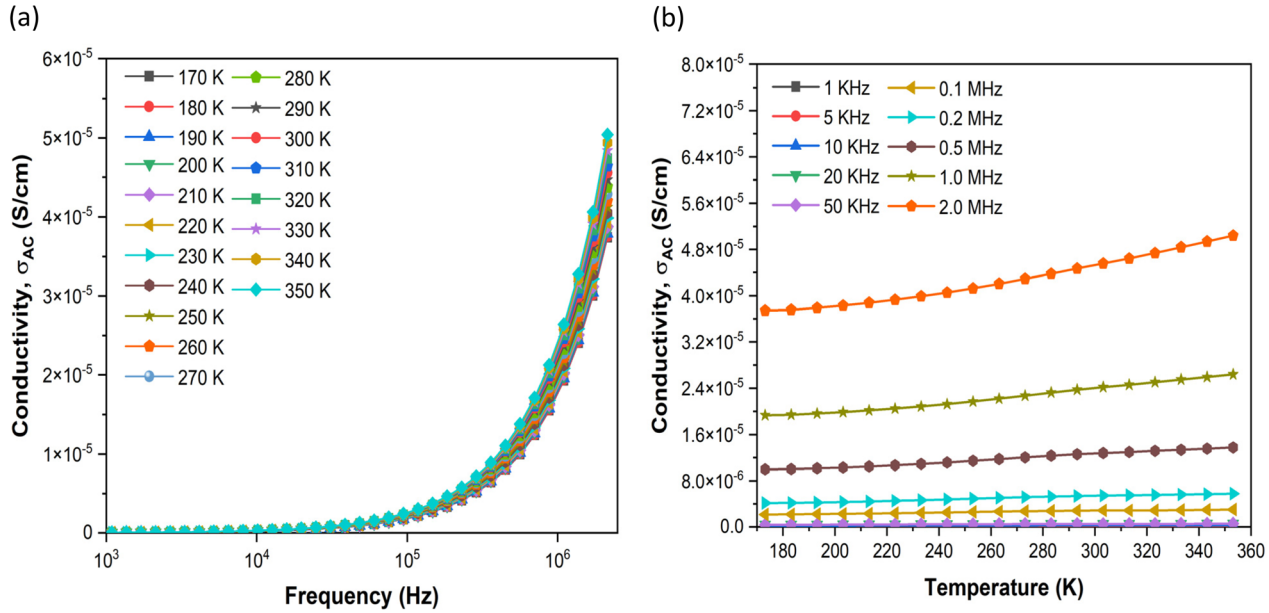

Fig. 8 (a) AC conductivity (σ_{AC}) *versus* frequency for ZnO NPs calcined at 500 °C, recorded over the measurement temperature range of 170–350 K and (b) AC conductivity (σ_{AC}) *versus* temperature for ZnO NPs calcined at 500 °C, recorded over the measurement frequency range of 10^3 to 10^6 Hz.

many materials, including polymers and semiconductors.[71] It was noted that the AC conductivity remained almost constant up to 10^4 Hz. Above 10^4 Hz, it gradually increased up to 10^5 Hz, and then, rose rapidly from 10^5 to 10^6 Hz. As the temperature increased, the AC conductivity (σ_{AC}) of ZnO NPs also increased due to the enhanced hopping of charge carriers.[72] At low frequencies, a feeble conductivity was attributed to the formation of less conductive grain boundaries, resulting from a limited number of charge carriers tunneling through the potential barrier.[73] However, an increment in the conductivity was observed due to a large number of charge carriers that could overcome the potential barrier at high frequency.[74] These results suggest that ZnO NPs exhibited frequency- and the temperature-dependent behavior characteristic of semiconductors.

The activation energy (E_a) of the semiconductivity of ZnO NPs was calculated with the use of the Arrhenius equation, $\sigma_{AC} = \sigma_0 \exp(-E_a/k_BT)$, where σ_0 is the pre-exponential factor, E_a is the activation energy, T is the temperature in kelvin, and k_B is the Boltzmann constant. Fig. 9 illustrates the plot of σ_{AC} *vs.* $10^3/T$ for ZnO NPs calcined at 500 °C from which the activation energy, E_a was determined to be 0.068 eV, corroborating the previous report.[75] This result provides a strong indication of the semiconducting nature of the ZnO NPs.

3.6 Optical band gap

The solid-state UV-visible absorption spectrum of the ZnO NPs calcined at 500 °C exhibited an absorption peak at <400 nm, corresponding to the electronic transition between the Zn_{3d} and O_{2p} states in hexagonal wurtzite ZnO NPs.[76] The optical band gap of the ZnO NPs was determined from the diffuse reflectance data using the Tauc relation:[77]

$$(\alpha h\nu) = B(h\nu - E_g)^n \quad (6)$$

where α is the absorption coefficient, B is a constant called the band tailing parameter, E_g is the optical band gap, h is the Planck's constant and ν is the frequency of incident photons, and 'n' is an index, which is equal to 2, 3, 1/2 and 1/3 for indirect allowed, indirect forbidden, direct allowed and direct forbidden transitions, respectively. We found that the only linear fit between $(\alpha h\nu)^n$ and $h\nu$ was obtained for $n = 1/2$, indicating a direct allowed transition[78] and the value of E_g obtained for this transition was 3.16 eV (Fig. 10), which is in agreement with the reported value of the band gap for ZnO NPs.[79] These findings

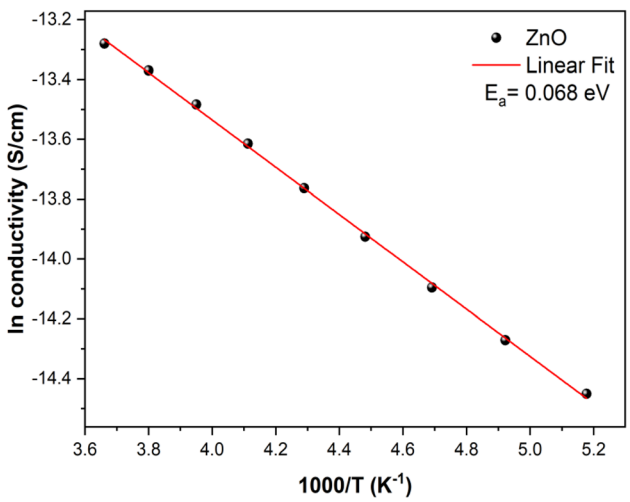

Fig. 9 Arrhenius plot of ln σ_{AC} *versus* 1000/T for ZnO NPs calcined at 500 °C, yielding an activation energy of 0.068 eV.

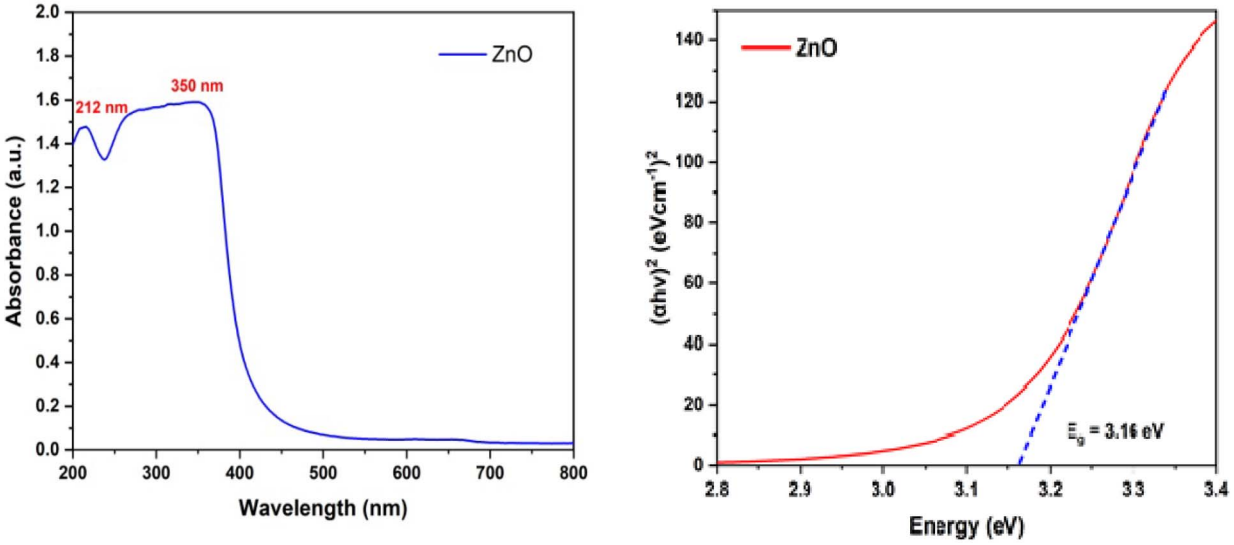

Fig. 10 (Left) UV-visible absorption spectrum, and (Right) UV-visible diffuse reflectance spectrum of ZnO NPs calcined at 500 °C. Tauc plot indicates a direct allowed band gap of 3.16 eV.

demonstrate that the ZnO NPs calcined at 500 °C are, indeed, promising materials for low-frequency devices, enhancing their performance and efficiency due to their improved dielectric characteristics and reduced energy gap.

Compared to earlier reports summarized in Table 1, ZnO NPs synthesized in this study exhibit a distinctive combination of properties. The crystallite size, ranging from 7 to 24 nm, is smaller than that of most co-precipitated or sintered samples, leading to enhanced grain boundary effects. This material is characterized by a high dielectric constant of approximately 98 at 10^3 Hz, coupled with a relatively low dielectric loss of about 0.96. This sets it apart from solution- and sol–gel-based ZnO NPs, which typically demonstrate lower dielectric constants and significantly higher losses. Moreover, while most studies do not provide impedance data, our work includes a detailed Nyquist analysis that clearly illustrates thermally activated hopping conduction. Alongside a direct band gap of 3.16 eV, these findings afford a deeper understanding of charge transport, grain boundary effects, and relaxation dynamics, thereby offering a more complete characterization than earlier studies. This thorough evaluation highlights the significant potential of ZnO NPs for advanced electronic technologies.

4. Conclusions

In this study, ZnO NPs were successfully synthesized by a simple, fast, cost-effective precipitation method, followed by calcination at 500 °C. XRD structural analysis confirmed the formation of highly crystalline ZnO with a hexagonal wurtzite structure with an average crystallite size of ~15.8 nm. SEM and particle size analysis revealed that the synthesized ZnO NPs possessed a nanostructured morphology, composed of multiple crystallites, which supports the existence of grain boundaries within each ZnO NPs. The optical characterization showed a direct band gap of 3.16 eV, consistent with quantum confinement in nanoscale ZnO. At a low frequency of 10^3 Hz, the ZnO NPs exhibited a high dielectric constant of 98 and a dielectric loss of 0.97. A decrease in both the dielectric constant and dielectric loss was observed with increasing frequency, likely due to the due to reduced interfacial polarization and formation of grain boundaries between ZnO NPs. Impedance spectroscopy confirmed the semiconducting nature of these nanoparticles, with temperature-dependent Nyquist plots showing enhanced charge carrier mobility at elevated temperatures. Electrical conductivity measurements showed an AC conductivity in the range of 10^{-8} to 10^{-5} S cm^{-1}, indicating that charge carrier mobility is primarily governed by thermally activated hopping mechanism. The calculated activation energy of 0.068 eV further supported the temperature-dependent conductivity behavior. These findings suggest that ZnO NPs calcined at 500 °C hold significant potential for the development of high-performance electronic devices.

Conflicts of interest

There are no conflicts to declare.

Data availability

The data supporting this article have been included in the experimental part and as part of the supplementary information (SI). Supplementary information: Tables S1–S7 and Fig. S1–S5. See DOI: https://doi.org/10.1039/d5ra06276d.

Acknowledgements

P. T. gratefully acknowledges Pondicherry University for providing financial support through the Start-Up Grant. A. Y. acknowledges Pondicherry University for the award of the Non-NET UGC Fellowship. We also thank the Central

Instrumentation Facility (CIF), Pondicherry University, for extending instrumental support and supplying data relevant to this study. Special thanks are due to Dr C. R. Mariappan, Department of Physics, Pondicherry University, for his assistance in acquiring the PXRD data.

References

1 A. Janotti and C. V. d. Walle, *Rep. Prog. Phys.*, 2009, **72**, 126501.
2 J. Zhou, N. S. Xu and Z. L. Wang, *Adv. Mater.*, 2006, **18**, 2432.
3 D. K. Sharma, S. Shukla, K. K. Sharma and V. Kumar, *Mater. Today: Proc.*, 2022, **49**, 3028.
4 T. Sarkar, S. Kundu and A. Bhattacharjee, *Phys. Status Solidi A*, 2024, **221**, 2300615.
5 D. Segets, J. Gradl, R. K. Taylor, V. Vassilev and W. Peukert, *ACS Nano*, 2009, **3**, 1703.
6 Z. L. Wang, X. Y. Kong, Y. Ding, P. Gao, W. L. Hughes and R. Yang, *Adv. Funct. Mater.*, 2004, **14**, 943.
7 Z. Deng, M. Chen, G. Gu and L. Wu, *J. Phys. Chem. B*, 2008, **112**, 16.
8 S. Raha and Md. Ahmaruzzaman, *Nanoscale Adv.*, 2022, **4**, 1868.
9 W. Guo, T. Liu, H. Zhang, R. Sun, Y. Chen, W. Zeng and Z. Wang, *Sens. Actuators, B*, 2012, **166–167**, 492.
10 H. Guo, J. Zhou and Z. Lin, *Electrochem. Commun.*, 2008, **10**, 1460.
11 O. Akhavan, M. Mehrabian, K. Mirabbaszadeh and R. Azimirad, *J. Phys. D:Appl. Phys.*, 2009, **42**, 225305.
12 J. M. Szarko, J. K. Song, C. W. Blackledge, I. Swart, S. R. Leone, S. Li and Y. Zhao, *Chem. Phys. Lett.*, 2005, **404**, 171.
13 P. Dhiman, G. Rana, A. Kumar, G. Sharma, D.-V. N. Vo and Mu. Naushad, *Environ. Chem. Lett.*, 2022, **20**, 1047.
14 M. Shoeb, S. Ahmad, F. Mashkoor, M. N. Khan, I. Hasan, B. R. Singh and C. Jeong, *J. Phys. Chem. Solids*, 2024, **184**, 111707.
15 Z. Wang, *Appl. Phys. A*, 2007, **88**, 7.
16 C. B. Onga, L. Y. Ng and A. W. Mohammad, *Renewable Sustainable Energy Rev.*, 2018, **81**, 536.
17 S. Nandi, S. Kumar and A. Misra, *Mater. Adv.*, 2021, **2**, 6768.
18 A. Wang, W. Quan, H. Zhang, H. Li and S. Yang, *RSC Adv.*, 2021, **11**, 20465.
19 S. Gunalan, R. Sivaraj and V. Rajendran, *Prog. Nat. Sci.:Mater. Int.*, 2012, **22**, 693.
20 A. Sirelkhatim, S. Mahmud, A. Seeni, N. H. M. Kaus, L. C. Ann, S. K. M. Bakhori, H. Hasan and D. Mohamad, *Nano-Micro Lett.*, 2015, **7**, 219.
21 V. Gerbreders, M. Krasovska, E. Sledevskis, A. Gerbreders, I. Mihailova, E. Tamanis and A. Ogurcovs, *CrystEngComm*, 2020, **22**, 1346.
22 P. Rai, W.-K. Kwak and Y.-T. Yu, *ACS Appl. Mater. Interfaces*, 2013, **5**, 3026.
23 T. A. Abdel-Baset and M. Belhaj, *Physica B*, 2021, **616**, 413130.
24 P. Banerjee, S. Chakrabarti, S. Maitra and B. K. Dutta, *Ultrason. Sonochem.*, 2012, **19**, 85.
25 K. Davis, R. Yarbrough, M. Froeschle, J. White and H. Rathnayake, *RSC Adv.*, 2019, **9**, 14638.
26 Y.-T. Tsai, S.-J. Chang, L.-W. Ji, Y.-J. Hsiao, I. T. Tang, H.-Y. Lu and Y.-L. Chu, *ACS Omega*, 2018, **3**, 13798.
27 N. Reuge, R. Bacsa, P. Serp and B. Caussat, *J. Phys. Chem. C*, 2009, **113**, 19845.
28 M. I. Khalil, M. M. Al-Qunaibit, A. M. Al-zahem and J. P. Labis, *Arabian J. Chem.*, 2014, **7**, 1178.
29 M. Hasanpoor, M. Aliofkhazraei and H. Delavari, *Procedia Mater. Sci.*, 2015, **11**, 320.
30 A. O. El-Gendy, K. T. Nawaf, E. Ahmed, A. Samir, M. R. Hamblin, M. Hassan and T. Mohamed, *J. Photochem. Photobiol., B*, 2022, **234**, 112540.
31 J. Gao, H. Ju, Z. Yao, G. Zhang, Q. Jiang and H. Guo, *Polym. Eng. Sci.*, 2023, **63**, 2204.
32 C. Ozel, C. K. Macit, T. Gurgenc, F. Biryan, E. Gurgenc and S. Bellucci, *Appl. Phys. A*, 2024, **130**, 232.
33 *In Zinc Oxide Materials for Electronic and Optoelectronic Device Applications*, ed. C. W. Litton, D. C. Reynolds and T. C. Collins, John Wiley & Sons, Chichester, West Sussex, PO19 8SQ, United Kingdom, 2011.
34 K. Sowmya, Y. Aparna, A. C. Prakash, R. Thotakura and A. Bhaskar, *Phys. Status Solidi A*, 2024, **221**, 2300628.
35 A. Sulciute, K. Nishimura, E. Gilshtein, F. Cesano, G. Viscardi, A. G. Nasibulin, Y. Ohno and S. Rackauskas, *J. Phys. Chem. C*, 2021, **125**, 1472.
36 N. Ahmed, Z. Khalil, Z. Farooq, Khizar-ul-Haq, S. Shahida, Ramiza, P. Ahmad, K. W. Qadir, R. Khan and Q. Zafar, *ACS Omega*, 2024, **9**, 137.
37 T. S. Velayutham, W. H. Abd Majid, W. C. Gan, A. Khorsand Zak and S. N. Gan, *J. Appl. Phys.*, 2012, **112**, 054106.
38 N. Ghifari, R. Bennacer, A. Chahboun and A. I. El Abed, *Micromachines*, 2022, **13**, 1522.
39 V. N. Hegde, V. V. Manju, T. M. Pradeep and B. C. Hemaraju, *J. Sci.:Adv. Mater. Devices*, 2024, **9**, 100733.
40 A. Muhammad, M. Sajid, M. N. Khan, M. Sheraz, A. Khalid, P. Ahmad, S. Alotibi, H. M. Al-saidi, N. Sobahi, Md. M. Alam, S. Althahban, A. M. Saeedi and H. B. Albargi, *PLoS One*, 2023, **18**, e0287322.
41 M. D. P. Ahmad, A. Venkateswara Rao, K. Suresh Babu and G. Narsinga Rao, *Mater. Chem. Phys.*, 2019, **224**, 79.
42 D. Kaur, A. Bharti, T. Sharma and C. Madhu, *Int. J. Opt.*, 2021, 9950202.
43 D. Raoufi, *Renewable Energy*, 2013, **50**, 932.
44 M. Goswami, N. C. Adhikary and S. Bhattacharjee, *Optik*, 2018, **158**, 1006.
45 R. Ashraf, S. Riaz, Z. N. Kayani and S. Naseem, *Mater. Today: Proc.*, 2015, **2**, 5468.
46 T. A. Abdel-Baset and M. Belhaj, *Physica B*, 2021, **616**, 413130.
47 G. Nagaraju, Udayabhanu, Shivaraj, S. A. Prashanth, M. Shastri, K. V. Yathish, C. Anupama and D. Rangappa, *Mater. Res. Bull.*, 2017, **94**, 54.
48 C. Mabrouk, J. Wannassi, P. A. S. Carballo, S. Carinelli, A. J. Gross, H. Kahri, N. Jaffrezic-Renault and H. Barhoumi, *Microchem. J.*, 2025, **212**, 113562.
49 A. M. Faramawy, W. R. Agami and M. A. Swillam, *Ceramics*, 2025, **8**, 2.

50 M. Karyaoui, A. Mhamdi, H. Kaouach, A. Labidi, A. Boukhachem, K. Boubaker, M. Amlouk and R. Chtourou, *Mater. Sci. Semicond. Process.*, 2015, **30**, 255.
51 G. Otis, M. Ejgenberg and Y. Mastai, *Nanomaterials*, 2021, **11**, 238.
52 A. Sahai and N. Goswami, *Ceram. Int.*, 2014, **40**, 14569.
53 J. Lee, J.-H. Hwang, J. J. Mashek, T. O. Mason, A. E. Miller and R. W. Siegel, *J. Mater. Res.*, 1995, **10**, 2295.
54 P. M. Shirage, A. K. Rana, Y. Kumar, S. Sen, S. G. Leonardi and G. Neri, *RSC Adv.*, 2016, **6**, 82733.
55 A. A. Al-Luhaibi, F. R. K. Sendi and J. Radiation Res, *Appl. Sci.*, 2024, **17**, 100909.
56 P. S. Chakra, A. Banakar, S. N. Puranik, V. Kaveeshwar, C. R. Ravikumar and D. Gayathri, *Beilstein J. Nanotechnol.*, 2025, **16**, 78.
57 S. B. Aziz, T. J. Woo, M. F. Z. Kadir and H. M. Ahmed, *J. Sci.:Adv. Mater. Devices*, 2018, **3**, 1.
58 S. N. Das, S. K. Pradhan, S. Bhuyan, S. Sahoo, R. N. P. Choudhary and M. N. Goswami, *J. Electron. Mater.*, 2017, **47**, 843.
59 P. Kumar, J. K. Juneja, C. Prakash, K. K. Raina and S. Singh, *Physica B*, 2013, **426**, 112.
60 A. Tripathy, S. N. Das, S. K. Pradhan, S. Bhuyan and R. N. P. Choudhary, *J. Mater. Sci.:Mater. Electron.*, 2018, **29**, 4770.
61 Z. M. Dang, Y. Q. Lin, H. P. Xu, C. Y. Shi, S. T. Li and J. Bai, *Adv. Funct. Mater.*, 2008, **18**, 1509.
62 M. M. Hassan, W. Khan, A. Azam and A. H. Naqvi, *Ind. Eng. Chem.*, 2015, **21**, 283.
63 K. Yang, X. Huang, Y. Huang, L. Xie and P. Jiang, *Chem. Mater.*, 2013, **25**, 2327.
64 N. H. Vinayakprasanna, V. V. Manju, T. M. Pradeep and B. C. Hemaraju, *J. Sci.:Adv. Mater. Devices*, 2024, **9**, 100733.
65 S. K. Barik, R. Choudhary and A. Singh, *Adv. Mater. Lett.*, 2011, **2**, 419.
66 M. Bastianello, S. Gross and M. T. Elm, *RSC Adv.*, 2019, **9**, 33282.
67 J. Song, E. Zheng, L. Liu, X. F. Wang, G. Chen, W. Tian and T. Miyasaka, *ChemSusChem*, 2016, **9**, 2640.
68 P. K. Kannan and R. Saraswathi, *J. Mater. Res.*, 2017, **32**, 2800.
69 J. Jose and M. Abdul Khadar, *Mater. Sci. Eng., A*, 2001, **304–306**, 810–813.
70 R. N. Aljawfi, F. Rahman and K. M. Batoo, *J. Mol. Struct.*, 2014, **1065–1066**, 199.
71 P. Dutta, S. Biswas, M. Ghosh, S. K. De and S. Chatterjee, *Synth. Met.*, 2001, **122**, 455.
72 S. Mahboob, G. Prasad and G. S. Kumar, *Bull. Mater. Sci.*, 2006, **29**, 347.
73 H. Saadi, F. I. H. Rhouma, Z. Benzarti, Z. Bougrioua, S. Guermazi and K. Khirouni, *Mater. Res. Bull.*, 2020, **129**, 110884.
74 M. Ashokkumar and S. Muthukumaran, *J. Lumin.*, 2015, **162**, 97.
75 Y. W. Heo, L. C. Tien, D. P. Norton, B. S. Kang, F. Ren, B. P. Gila and S. J. Pearton, *Appl. Phys. Lett.*, 2004, **85**, 2002.
76 G. Vijayaprasath, R. Murugan, S. Asaithambi, G. AnandhaBabu, P. Sakthivel, T. Mahalingam, Y. Hayakawa and G. Ravi, *Appl. Phys. A*, 2016, **122**, 122.
77 H. Saadi, Z. Benzarti, S. Mourad, P. Sanguino, Y. Hadouch, D. Mezzane, N. Abdelmoula and H. Khemakhem, *J. Mater. Sci.: Mater. Electron.*, 2022, **33**, 8065.
78 S. A. Ansari, A. Nisar, B. Fatma, W. Khan and A. H. Naqvi, *Mater. Sci. Eng., B*, 2012, **177**, 428.
79 K. W. Aga, M. T. Efa and T. T. Beyene, *ACS Omega*, 2022, **7**, 10796.
80 F. Tezcan, A. Mahmood and G. Kardaş, *J. Mater. Sci.: Mater. Electron.*, 2018, **29**, 9547–9554.
81 M. Chaari and A. Matoussi, *Phys. B*, 2012, **407**, 3441.
82 A. Kołodziejczak-Radzimska, E. Markiewicz and T. Jesionowski, *J. Nanomater.*, 2012, 656353.
83 T. Sarkar, S. Kundu and A. Bhattacharjee, *Phys. Status Solidi A*, 2024, **221**, 2300615.
84 E. Silva and A. Franco, *J. Eur. Ceram. Soc.*, 2020, **40**, 1307.
85 S. Ibadat, M. Younas, S. Shahzada, M. Nadeem, T. Ali, M. J. Akhtar and R. T. A. Khan, *RSC Adv.*, 2020, **10**, 30451.
86 S. Sagadevan, S. Vennila, J. A. Lett, A. R. Marlinda, N. A. B. Hamizi and M. R. Johan, *Results Phys.*, 2019, **15**, 102543.
87 A. S. Lanje, S. J. Sharma, R. S. Ningthoujam, J. S. Ahn and R. B. Pode, *Adv. Powder Technol.*, 2013, **24**, 331.
88 V. N. Hegde, *J. Sci.:Adv. Mater. Devices*, 2024, **9**, 100733.